Overall water splitting realized by overall sputtering thin-film technology for a bifunctional MoNiFe electrode: A green technology for green hydrogen

Noto Susanto Gultom [a], Tien-Shin Chen [a], Mikha Zefanya Silitonga [a], Dong-Hau Kuo [a,b,*]

[a] *Department of Materials Science and Engineering, National Taiwan University of Science and Technology, No. 43, Section 4, Keelung Road, Taipei 10607, Taiwan*
[b] *Graduate Institute of Energy and Sustainability Technology, National Taiwan University of Science and Technology, No. 43, Section 4, Keelung Road, Taipei 10607, Taiwan*

ABSTRACT

Electrode for water electrolysis needs to be prepared by a non-traditional way to overcome the peel-off problem of electrocatalysts under high current. Herein, we use the sputtering technology to prepare the ternary MoNiFe alloys with various Mo contents as bifunctional electrocatalyst for overall water splitting in alkaline solution. The incorporation of Mo atoms in the NiFe host structure improved the hydrogen evolution reaction (HER) and the oxygen evolution reaction (OER) performance. The bifunctional MNF-2 electrolyte cell requires a cell potential of 1.55 V at 10 mA/cm^2. The scale-up single MNF-2 stack cell of 3×3 cm^2 needed 1.9 and 2.1 V to reach 100 and 500 mA/cm^2, respectively. Stability test at 100 mA/cm^2 for 100 h showed no degradation. The sputtering thin-film technology can not only deposit excellent catalyst but also provide the strong catalyst/support adherence for industrial application. The excellent activity of MoNiFe is attributed to its composition design.

1. Introduction

Electrolytic water splitting is one of the most effective and eco-friendly techniques for large-scale hydrogen production. It consists of two reactions of hydrogen evolution reaction (HER) and oxygen evolution reaction (OER) at the cathode and anode electrodes, respectively [1]. Theoretically, a potential of 1.23 V is required to drive electrolytic water splitting [2]. However, the input potential is larger than 1.23 V in practical application due to a relatively high overpotential to overcome the sluggish kinetic reactions of both HER and OER [3]. The platinum group and iridium/ruthenium-based materials continue to be the state-of-the-art catalysts for HER and OER, respectively [4,5]. Unfortunately, their high cost and scarcity are the main obstacles for commercial production. Therefore, the efforts on searching active and efficient catalysts with low cost, earth abundant constituents such as Ni, Fe, and Mo, and low overpotential are still the major research focuses in this field.

The surface area of an electrocatalyst has been regarded as a crucial feature that considerably affects its performance. Previous research has demonstrated that nano-structuring such as nanosheets, nanorods, nanowires, and nanospheres [6–9] can increase the geometric surface area and catalyst activity. However, not only the quantity but also the quality of surface areas is highly crucial for determining the electrochemical performance [10]. A key strategy to improve the quality of surface areas in order to make them electrochemically active for reactions is by tuning the element composition [11]. By selecting the proper elements and their concentrations, it is highly possible to generate a high-performance electrocatalyst, like bimetal and trimetal alloys. Apart from the nano-structuring and tuning of element composition, the preparation process of electrocatalysts is also a crucial factor for the practical application. Hydrothermal method and pyrolysis are two of the most commonly used methods to synthesize electrocatalysts [12,13]. Unfortunately, these methods require a lengthy synthesis process, involve the use of toxic chemicals, have difficulty in scale-up with uniformity, and suffer from the crystal/substrate adherence problem at high current density. The issue of crystal/substrate adherence has to be pointed out here. During the high gas output, the intermittent bubble buoyant force has a stronger impact on the 3D standing nanostructured electrodes. For a standard test of water splitting at 10 mA/cm^2, the peel-off problem of electrocatalysts is not an issue. However, to build a

---

new electrolytic cell in an alkaline solution at an industrial scale, the catalyst design strategy needs to seriously consider the adherence issue.

Herein, the sputtering thin-film technique is proposed as an alternative method to prepare an efficient, inexpensive, bifunctional, and strongly adherent electrocatalyst for cathode, anode, and full cell water electrolysis. The sputtering process has many advantages, such as the excellent adhesion between the thin film and the substrate without the use of binders, a green process without the use of toxic or hazardous chemicals, a dry process without liquid wastes, a scalable technique for mass production, and an adjustable process in composition and uniformity [14]. Using this thin-film technology to synthesize water splitting electrocatalysts is expected to solve the peel-off problem due to the plasma aid in forming strong film/substrate bonding. There are few reports to show the stability of water-splitting electrocatalysts operated at 1000–2000 mA/cm^2 without degradation [15,16]. There are also limited literatures on the sputtered electrocatalysts for water splitting. To demonstrate the stability of electrocatalytic electrodes for water splitting sustained at 1–2 A/cm^2 without degradation is a challenging research toward the feasible industrial applications.

The goals of this work are to have the sputtered electrocatalysts for HER and OER in an alkaline electrolyte, and to demonstrate a 1×1 cm^2 electrolytic cell and a scale-up 3×3 cm^2 single stack cell made all by the sputtering thin-film technology. A bifunctional trimetal system of MoNiFe was targeted. The best performance for HER and OER was surveyed by adjusting the target composition. The sample of MNF-2 deposited with the target of Mo:Ni:Fe at 0.25: 1: 1 achieved the best for HER and OER. That MNF-2 requires overpotentials of 139 and 273 mV for HER and 238 mV and 295 mV for OER to attain current densities of 10 and 100 mA/cm^2, respectively. The scale-up single stack cell is built to evaluate the electrode scalability with cell potentials of 1.9 and 2.1 V to achieve high current densities at the industry level of 100 and 500 mA/cm^2, respectively. The cells did not show any degradation under stability test at 100 mA/cm^2 for 100 h. The post-characterizations reveal that the formation of in-situ nickel oxyhydroxide occurred during the OER test, which was responsible as the active side for the OER, whereas the as-sputtered MoNiFe alloy served as the active HER catalyst. To challenge the operation at high current density, we will demonstrate the excellent performance of the electrocatalyst at 2000 mA/cm^2 without degradation. The excellent water splitting performance for the sputtered MoNiFe thin films with a dense and smooth morphology was explored and explained, based upon the microstructural, composition, and electrochemical characterizations.

2. Experimental section

2.1. Sputtering target preparation

MoNiFe alloy sputtering targets were home-made using a hot-press machine with various Mo ratios, including Mo$_0$NiFe, Mo$_{0.125}$NiFe, Mo$_{0.25}$NiFe, and Mo$_{0.5}$NiFe, which were further denoted as MNF-0, MNF-1, MNF-2, and MNF-3, respectively. Briefly, commercial nickel, iron, and molybdenum powders were homogenously mixed for 12 h using a dry ball milling process. The as-mixed powders were then carefully poured into a graphite mold with a copper plate as the back support. After that, the mold was transferred into the chamber of the hot-press machine. After approximately 30 min of pumping, the chamber was refilled with argon while the pump was turned off. The hot-press procedure was performed at 400 ºC for 30 min under 300 psi of hydraulic pressure. After allowing the target to cool down naturally, it was carefully taken from the mold and polished with sand paper.

2.2. Magnetron sputtering

Prior to the sputtering process, the sputtering chamber was firstly evacuated to a low vacuum with a rotary pump, and then to a high vacuum with a turbomolecular pump for 1 h until the pressure reached

10^{-6} torr. After that, the pre-sputtering was conducted at a low power of 30 watts for about 20 min to remove the surface contamination. Keeping a working distance of 10 cm from the substrate, the target was then sputtered at 300 °C with a power of 70 watts for 30 min. The entire sputtering procedure was carried out with argon as the working gas at a pressure of 9.5×10^{-3} torr.

2.3. Electrochemical analysis

The HER or OER half reaction was evaluated using a three-electrode configuration, with the as-sputtered MoNiFe on Ni-foam serving as the working electrode (1 cm^2), the Hg/HgO (filled with 1 M KOH) as the reference electrode, and the platinum foil as the counter electrode (2 cm^2) in a 1 M KOH electrolyte. All the potential given in this work was translated to the RHE according to our earlier publication [17]. The performance of the as-sputtered MoNiFe electrode was assessed using the linear sweep voltammetry (LSV) method with potential ranges of $-0.4 \sim 0$ and $1.2 \sim 2.0$ V vs. RHE for HER and OER, respectively. The overall water splitting test was performed using a two-electrode system, where the best catalyst for HER and OER served as both anode and cathode electrodes. All the LSV curves were measured with IR-compensation at a level of 85%.

2.4. Characterizations

X-ray diffraction patterns were taken using X-ray diffractometer (D2, phase) with Cu Kα ($\lambda = 1.54$ Å) at an operating voltage of 30 kV. The surface morphology of the samples was observed using a field emission scanning electron microscope (FE-SEM, JEOL 6500). Transmission electron microscopy (TEM) was performed on the FEI Talos F200X at an accelerating voltage of 200 kV. X-ray photoelectron spectroscopy (XPS) was conducted using a PHI 5000 Versa Probe III (ULVAC-PHI) with Al K$_\alpha$ to investigate the chemical states. Prior to the XPS measurement, the sample was pretreated with argon ion bombardment to cleanse the surface. A Raman analysis was performed using HORIBA (iHR550) with an excitation wavelength of 532 nm to examine the structure of the catalyst after being tested for OER and HER.

3. Results and discussion

3.1. X-ray diffraction and microstructure analyses

The crystal properties of the as-sputtered MoNiFe alloy were investigated by X-ray diffraction technique. For this purpose, Si wafer was chosen as the substrate instead of Ni foam to avoid the strong diffraction peaks from Ni substrate. As exhibited in Fig. S1, the representative X-ray diffractions of MNF-0 and MNF-2 have no visible peaks, similar to the spectrum from Si substrate. This result suggests that the as-sputtered MoNiFe alloy has an amorphous nature without any regular atomic arrangement. The surface of the as-sputtered MNF-*n* films with $n = 0$, 1, 2, and 3 was first observed using a scanning electron microscope. All the as-sputtered MoNiFe-alloy clearly shows a flat, smooth, and compact surface with fine granular particles that are uniformly coated throughout the nickel foam substrate, as depicted in Fig. 1a-d. The surface of MoNiFe electrodes seems similar with various Mo ratios even at a higher magnification, as depicted in Fig. 1e-g. TEM analysis was further conducted to investigate the nanostructure property of that MNF-2 catalyst. For this purpose, the TEM specimen was cut using focus ion beam (FIB) technology to get the cross-section image, as exhibited in Fig. 2a. The presence of Pt in Fig. 2a was to shield the specimen from the gallium ion-bombardment during the cutting procedure. Based on this image, the thickness of the catalyst can be precisely calculated to be about 140 nm. Fig. 3b shows the high-resolution transmission electron microscope (HRTEM) image. It can be clearly seen that there is no regular arrangement of atoms, indicating the amorphous nature. The selected area electron diffraction (SAED) pattern of MNF-2 in Fig. 2c
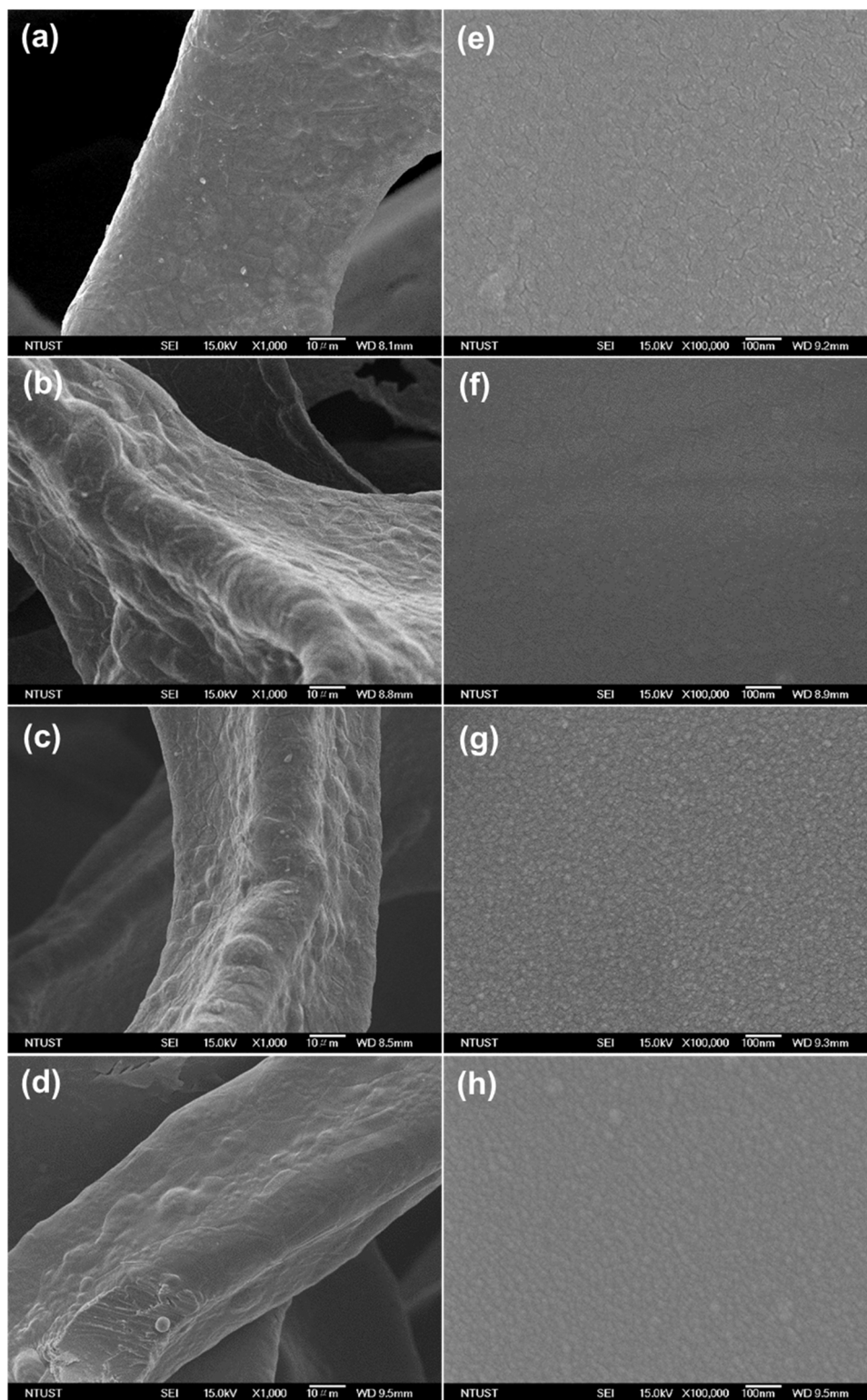
Fig. 1. FE-SEM images of (a,e) MNF-0, (b,f) MNF-1, (c,g) MNF-2 and (d,h) MNF-3 at (a-d) low and (e-h) high magnifications.

displays a blurry image rather than a ring or dot pattern, which further confirms the amorphous nature and is consistent with the XRD data. To investigate the elemental distributions of Mo, Ni, and Fe, the elemental mapping signal was acquired with a scanning transmission electron microscope (STEM) mode from the high-angle annular dark-field (HAADF) image in Fig. 3a. Fig. 3b-d shows that Ni, Fe, and Mo are homogenously spread out through the sample, with less signal intensity of the Mo element due to its much lower concentration than that of Ni or Fe. With the microstructure observations, sputtered MoNiFe films are dense, smooth, and uniform composition. The MoNiFe films did not have the 3D architectures such as nanosheet, nanorod, nanocube, nanoarray, nanowire, and so on to increase its geometric surface area.

The element composition of the as-sputtered MoNiFe alloy was quantitatively determined using an energy-dispersive X-ray
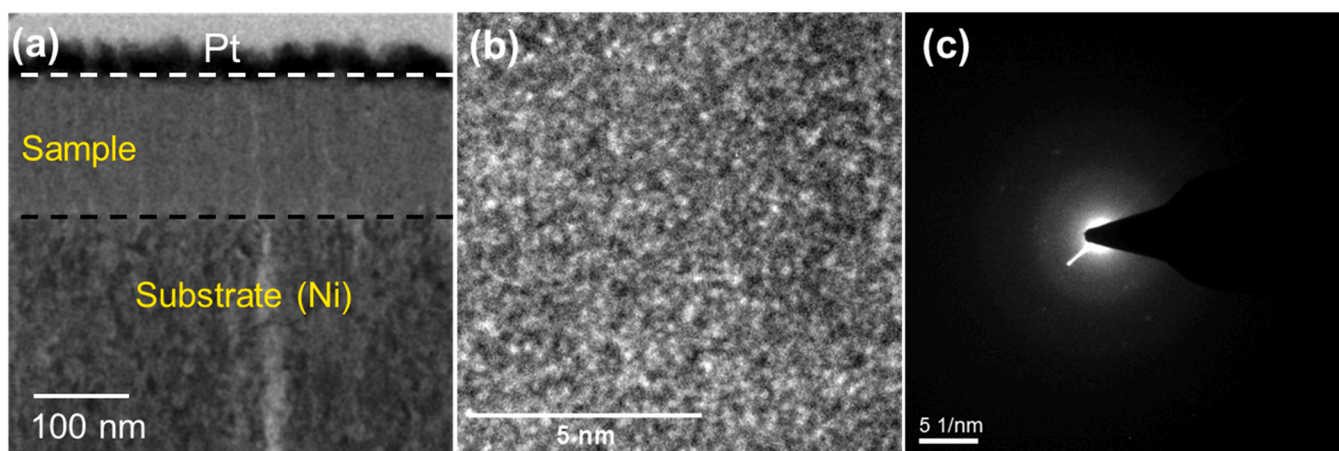
Fig. 2. (a) Transmission electron microscope image, (b) high-resolution TEM image, and (c) selected area electron diffraction (SAED) of MNF-2.
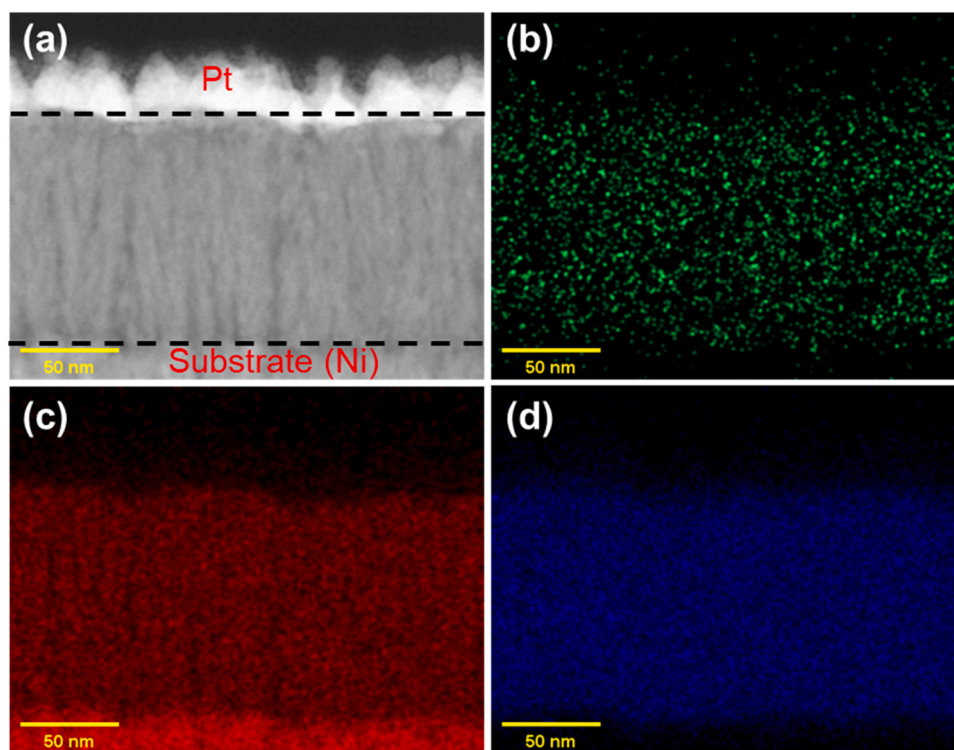
Fig. 3. (a) High-angle angular dark field (HAADF) image and elementals mapping of (b) molybdenum, (c) nickel, and (d) iron of MNF-2.

spectroscopy (EDS) analysis under a high probe current of 10 μA. Table 1 tabulates the atomic percentages of Ni, Fe, and Mo in MoNiFe for various Mo ratios. The atomic percentages of Ni and Fe on the as-sputtered MNF-0 were 59.28% and 40.72%, respectively. Then, the actual ration of Ni:Fe was 1:0.68, which was slightly different from the sputtering target with a ratio of 1:1 due to Ni having a slightly higher

sputtering yield than Fe [18]. After a small amount of Mo was incorporated into the NiFe host, the actual ratio of Mo: Ni: Fe in the MNF-1 catalyst became 0.15: 1: 0.87, which was also not much different from the target ratio of 0.125:1:1. As can be seen in Table 1, the atomic percentage of Mo in MNF-1, MNF-2, and MNF-3 gradually increases from 7.43% to 12.34%, and 22.10%, respectively. Based on this EDS data, the Mo ratios relative to Ni were 0.15, 0.27, and 0.48, which were similar to the ratios in the targets of 0.125, 0.25, and 0.5, respectively.

3.2. X-ray photoelectron spectroscopy (XPS) analysis

The surface chemistry of our MNF-2 was assessed by XPS analysis. The wide scan spectrum in Fig. 4a confirms the presence of our ternary alloy, including Mo 2p, Ni 2p, and Fe 2p. The XPS wide scan also exhibits the presence of O1s and C1s due to the well-known oxygen adsorption and carbon contamination from the air. Fig. 4b exhibits the high-

Table 1
Atomic percentage of MoNiFe alloy with various Mo ratios.

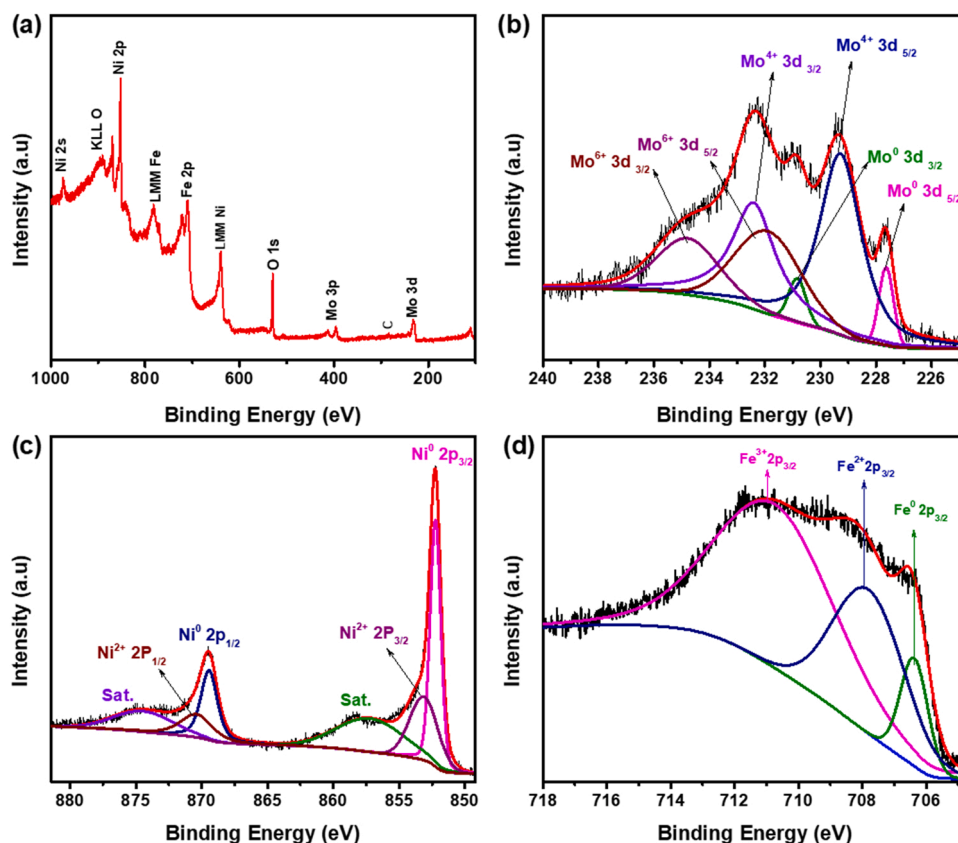| Catalyst	Atomic percentage (%)			Mo: Ni: Fe ratio		
	Mo	Ni	Fe	Target	Film	
MNF-0	–	59.28	40.72	-: 1:1	-: 1:0.68	
MNF-1	7.43	49.60	42.98	0.125:1:1	0.15:1:0.87	
MNF-2	12.34	46.56	41.10	0.25:1:1	0.27:1:0.88	
MNF-3	22.10	45.57	32.33	0.5:1:1	0.48:1:0.71	

Fig. 4. X-ray photoelectron spectroscopy (XPS) analysis of MNF-2 displayed with (a) a wide scan, and high-resolution spectra of (b) Mo 3d, (c) Ni 2p, and (d) Fe 2p.

resolution XPS spectra of Mo 3d. The binding energies of 227.6 and 230.7 eV indicate the existence of metallic Mo for spin-orbitals of Mo° $3d_{5/2}$ and Mo° $3d_{3/2}$, respectively [19]. It is also clear that there are other peaks at binding energies of 229.2 eV and 232.3 eV that correspond to the presence of Mo^{4+} $3d_{5/2}$ and Mo^{4+} $3d_{3/2}$, respectively [20]. With weaker peak intensity, the spin orbitals of Mo^{6+} $3d_{5/2}$ and Mo^{6+} $3d_{3/2}$ can be found at binding energies of 231.8 and 234.9 eV, respectively [21]. The high-resolution XPS spectra of Ni 2p in Fig. 4c shows the presence of Ni metal with binding energies of 852.5 and 869.7 eV for Ni° $2p_{3/2}$ and Ni° $2p_{1/2}$, respectively [22]. The additional peaks with binding energies of 853.3 and 870.6 eV correspond to the bivalent Ni^{2+} $2p_{3/2}$ and Ni^{2+} $2p_{1/2}$, respectively [23]. Ni $2p_{3/2}$ and Ni $2p_{1/2}$ have satellite peaks with binding energies of 857.4 and 874.7 eV, respectively. Fig. 4d demonstrates the asymmetric XPS peak of Fe $2p_{3/2}$, indicating the presence of several peaks with different oxidation states. After deconvolution, the peaks at binding energies of 706.5, 708.0, and 710.9 eV can be attributed to the presence of Fe with oxidation states of 0, 2 + , and 3 + , respectively [24]. Despite the presence of metallic Mo, Ni, and Fe signatures, the formation of the metals at their higher oxidation states, such as 2 + , 3 + , 4 + , and 6 + , can be attributed to the surface oxidation [25], which led Mo to Mo^{4+} and Mo^{6+}, and Fe to Fe^{3+} and Fe^{2+}, but had no big effects on Ni due to its better oxidation resistance [26], which gives a hint that the Mo and Fe are close to each other for reactions to occur. Based upon the phase diagrams and the amount of charge state, the as-deposited MoNiFe film involves the uniformly distributed phases of Ni, Ni-Fe, and Fe-Mo phases. After partial surface oxidation of $FeNi_3$ and the $FeMo_{1-y}$ intermetallic μ phase, as referred to the phase diagrams [27,28] to form the valence states, the non-stoichiometric Fe_3O_{4-x} corresponding to Fe^{2+} and Fe^{3+} and MoO_y compounds related to Mo^{4+} and Mo^{6+} are formed in the Ni matrix with oxygen deficient/vacancy at room temperature, as supported by the XPS data in Fig. 4 and Table S1. This type of surface oxidation is similar to the Al and Ti alloy to form a thin oxide layer for protection with the

difference in electrical conductivity as $Mo^{4+}O_{2-x}$ compound has a metal behavior. The metallic and oxidation-resistant $Mo^{4+}O_{2-x}$ plays a key role in a redox environment like electrodes for cathode and anode.

3.3. Electrocatalytic performance

3.3.1. Hydrogen evolution reaction

The performance of our MoNiFe alloy was initially tested toward the hydrogen evolution reaction (HER) in alkaline electrolyte of 1 M KOH at room temperature. As shown in Fig. 5a, the LSV curves demonstrate that the HER activity of MNF-0 without the addition of Mo metal is quite low. Its overpotential to attain a current density of − 10 mA/cm² was − 265 mV. Moreover, it was incapable of reaching a high current density of 100 mA/cm² at the same potential as other catalysts. With the addition of a small amount of Mo, the performance of MNF-1 greatly improved with the shifting of the polarization curve to a more positive potential. The overpotentials of MNF-1 to attain current densities of − 10 and − 100 mA/cm² were − 185 mV and − 314 mV, respectively. Surprisingly, that MNF-2 with a higher Mo content also shows a much better performance than those MNF-1 and MNF-0. It only takes overpotentials of − 139 and − 273 mV to attain current densities of − 10 and − 100 mA/cm², respectively. However, as the amount of Mo metal further increased in MNF-3, the HER performance began to decline, but remained better than that of MNF-0. The higher Mo content can form metal oxide (MoO_y) in a large degree to cover the active sites from Ni matrix, which can induce higher electron transfer resistance, as evidenced by the EIS analysis in the next section. The HER performance of our MNF-2 catalyst with an overpotential of 273 mV at a current density of 100 mA/cm² was compared to other HER catalysts prepared by the sputtering technique such as WSe_2 (350 mV) [29], Ni_2N (300 mV) [30], $Ag_2S-MoS_x/MoNiAg$ (285 mV) [31], and $CuCo_2S_4/FeO$ (220 mV) [32]. The stability of MNF-2 as the best HER catalyst was then evaluated using the chronopotentiometry technique [33]. The chronopotentiometric
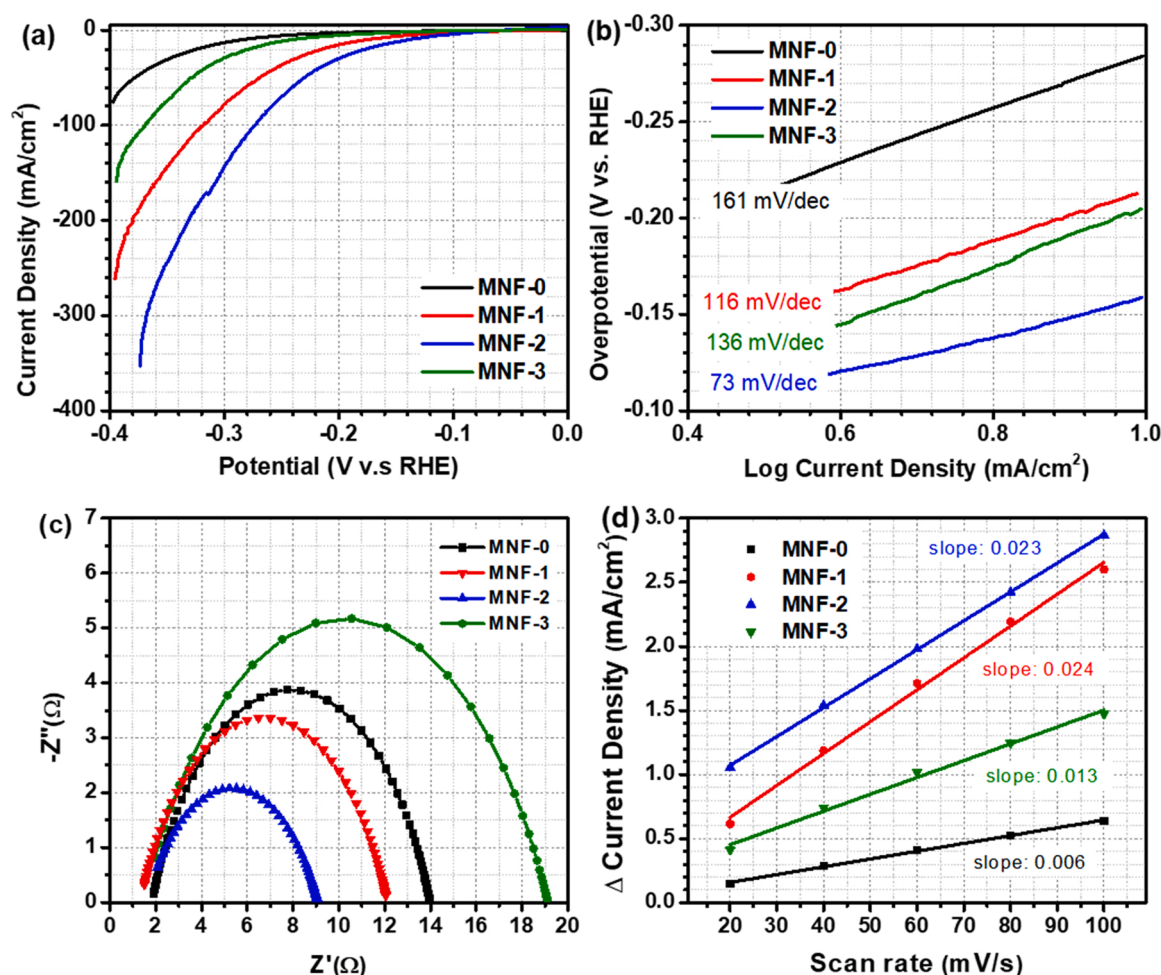
Fig. 5. (a) Hydrogen evolution polarization curves, (b) corresponding Tafel plot, (c) electrochemical impedance spectroscopy (EIS), and (d) plot of current density vs. scan rate to estimate the capacitive double layer (C_{dl}) of MoNiFe with various Mo ratios.

curve in Fig. S2 exhibits negligible potential variation against time, indicating stable performance. The HER activity of MNF-2 was further evaluated at different pH values of 12.5, 13.0, 13.4, and 13.8, as shown in Fig. S3. It is clear that the HER activity of our MNF-2 is pH dependent with a slope value of 0.6, as demonstrated in Fig. S4.

In order to assess the kinetic reaction of the as-sputtered MoNiFe alloy, the Tafel slope was firstly derived from the LSV data and plotted in Fig. 5b. The computed Tafel values for MNF-0, MNF-1, MNF-2, and MNF-3 were 161, 116, 73, and 136 mV/dec, respectively. It is obvious that the Tafel slope value is lowered for all samples with the addition of Mo metal. Especially for MNF-2, the Tafel value decreases from 161 to 73 mV/dec, revealing that the incorporation of Mo atoms into the NiFe system plays an important role in significantly boosting the kinetic reaction. The Tafel value of MNF-2 was the smallest among the as-sputtered MoNiFe alloys, suggesting the most favorable kinetic reaction. To further study the kinetic behavior of MNF-*n*, the EIS measurement was conducted by introducing an additional potential of -180 mV at a frequency range of 200 kHz to 100 mHz. The Nquist plot in Fig. 5c obviously exhibits the perfect semicircles with different diameters, which is proportional to the electron transfer resistance (R_{ct}). After fitting to a circuit model, the values of R_{ct} could be determined to be 12.15, 8.42, 7.48, and 17.68 Ω for MNF-0, MNF-1, MNF-2, and MNF-3, respectively. With an optimum Mo: Ni: Fe molar ratio, it is clear that a low charge transfer resistance can be achieved. To evaluate the effect of tuning element composition on the electrochemical active site, the CV curves at various scan rates were initially acquired at non-faradaic current, as shown in Fig. S5. Based on these data, the double layer

capacitance (C_{dl}) was computed from the slope of delta current density vs. scan rate, as plotted in Fig. 5d. The C_{dl} values of MNF-0, MNF-1, MNF-2, and MNF-3 were 6, 24, 23, and 13 mF/cm^2, respectively. The real electrochemical active surface area (ECSA), which is proportional to the capacitive double layer area, was then estimated by dividing the C_{dl} value with a specific capacitance (C_s). The standard C_s value of 0.04 mF/cm^2 per cm$^2_{ECSA}$ was chosen for the flat surface electrode in the alkaline solution [34]. Then, the ECSA value of MNF-2 was 575 cm^2, which was comparable to that of MNF-1 (600 cm^2) but much higher than MNF-0 of 150 cm^2 and MNF-3 of 325 cm^2. To compare the intrinsic activity, the LSV curve was then normalized to the ECSA value [35]. As presented in Fig. S6, MNF-2 also demonstrates much better HER activity as compared to other catalysts, indicating its great intrinsic activity. Furthermore, the turnover frequency (TOF) per active site was calculated, as shown in the supporting information. The TOF values of MNF-2 were 0.106 and 0.558 H$_2$/s at overpotentials of -0.2 and -0.3 V, respectively. These values are significantly greater than the TOF of MNF-0 and MNF-3, suggesting significantly greater activity. Here, both of the ECSA and TOF values show as clear indicators for HER activity. The electrolytic HER performance of the MoNiFe alloy with various Mo ratios is summarized in Table 2.

3.3.2. Oxygen evolution reaction

The electrocatalytic activity of MoNiFe alloy with various Mo molar ratios was further evaluated for OER under the same conditions as the HER test in the previous part. Surprisingly, the incorporation of Mo atoms into NiFe host materials can also significantly improve OER

Table 2
Summary of electrocatalytic HER performance of MoNiFe alloy with various Mo ratios.

Sample	Overpotential (V vs. RHE)		Tafel slope (mV/dec)	Charge transfer resistance (Ω)	ECSA (cm^2)	TOF at potentials $-0.2/$ -0.3 V
	-10 mA/ cm^2	-100 mA/ cm^2				
MNF-0	-0.265	N/A	161	12.15	150	0.045/ 0.253
MNF-1	-0.185	-0.314	116	8.42	600	0.073/ 0.374
MNF-2	-0.139	-0.273	73	7.48	575	0.107/ 0.558
MNF-3	-0.194	-0.345	136	17.68	325	0.048/ 0.261

performance, as evidenced by the shift of LSV curves to a more negative potential. As can be seen clearly in Fig. 6a, our MNF-2 catalyst shows much better OER performance than that of MNF-0 and is comparable to that of MNF-1. The overpotential of MNF-2 to achieve a high current density of 100 mA/cm^2 was 295 mV, which was much lower than that of MNF-0 (363 mV) or MNF-3 (346 mV). The reduction peak at a potential of 1.25 V vs. RHE corresponds to the reduction of Ni^{3+} to Ni^{2+} as the LSV recorded in the negative direction [36]. The OER activity of MNF-2 was also evaluated at different pH values, similar to the HER test. Fig. S7 clearly shows that the OER performance of the MNF-2 catalyst is also strongly pH dependent. Furthermore, the plot of log current density at a

potential of 1.58 V (vs. RHE) against pH value in Fig. S8 to obtain the reaction order (ρ) demonstrates a linear relationship with a slope value of 1.20, suggesting the presence of a non-concerted proton electron transfer (n-CPET) step during the OER [37]. The Tafel slope for OER is also calculated and plotted in Fig. 6b to further evaluate the OER kinetic. MNF-2 had a Tafel value of 33.8 mV/dec, which was quite similar to that of MNF-1 (38.1 MV/dec), but MNF-0 and MNF-3 had higher values of 48.1 and 46.2 mV/dec, respectively. Based on these results, the Tafel value of MNF-2 was the lowest, which suggests that it was the most efficient electrocatalyst at executing the oxidation reaction. Furthermore, the EIS analysis was further performed by applying a positive potential of 1.52 V vs. RHE to study the electron transfer during the OER. The results are presented in Fig. 6c. After analyzing the raw data, the charge transfer resistance for MNF-0, MNF-1, MNF-2, and MNF-3 was then estimated to be 1.413, 1.21, 1.012, and 1.231 Ω, respectively. The stability test of the MNF-2 catalyst for OER at a current density of 20 mA/cm^2 is quite stable, as shown in Fig. 6d. The OER LSV normalized to the ECSA value in Fig. S9 demonstrates the best OER performance of MNF-2, reflecting good intrinsic activity for OER. The TOF value of MNF-2 at a potential of 1.53 V was calculated to be 0.437 O_2/s, which was close to that of MNF-1 (0.391 O_2/s) and larger than those of MNF-0 (0.226 O_2/s) and MNF-3 (0.246 O_2/s). The performance of our MNF-2 with an overpotential of 280 mV at 100 mA/cm^2 for OER was comparable to some OER catalysts made by the sputtering technique, such as $CuCo_2S_4$/FeO (300 mV) [38], Ag-MoS_2 (370 mV) [39], CoNiFe oxide (315 mV) [40], and Co_3O_4-Fe_2O_3 (470 mV) [41].
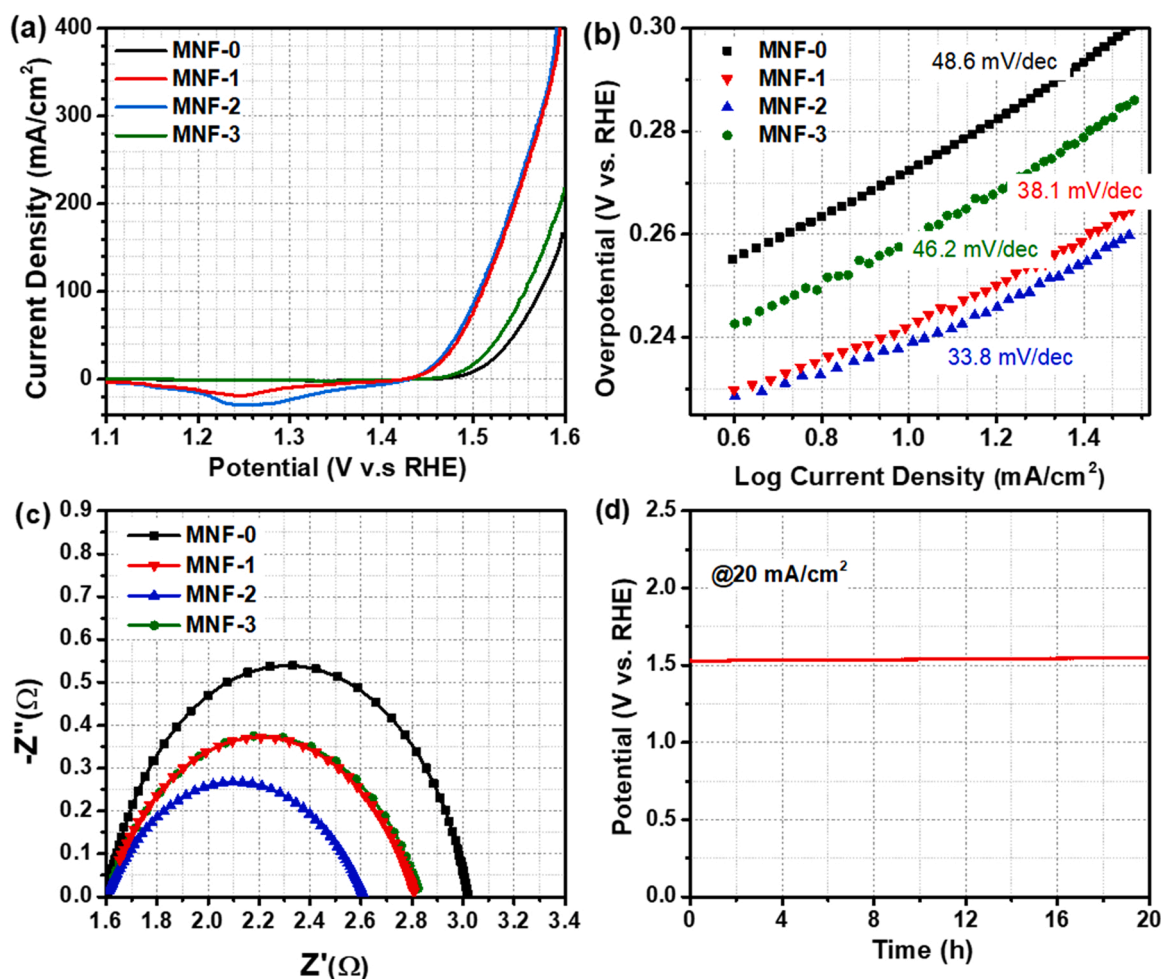
Fig. 6. (a) Oxygen evolution polarization curves, (b) corresponding Tafel plot, (c) electrochemical impedance spectroscopy (EIS) of MoNiFe with various Mo ratios, and (d) stability test of MNF-2.

3.3.3. Overall water splitting

Inspired by the great performance of our NFM-2 for both HER and OER, that catalyst was then subsequently used as the anode and cathode electrodes to drive overall water splitting in a single cell without a membrane, as illustrated in Fig. S10. The LSV curve in Fig. 8a shows that our NFM-2 requires cell potentials of 1.55 and 1.82 V to reach current densities of 10 and 100 mA/cm^2, respectively. To compare the performance of our MNF-2 with the benchmark catalysts, RuO_2 and Pt/C were used as the anode and cathode, respectively. As also shown in Fig. 7a, their cell potentials are 1.6 and 1.8 V at current densities of 10 and 100 mA/cm^2, respectively, which is similar to our MNF-2. As stability is one of the very important features needed to consider for the real application, the stability of our MNF-2 catalyst was then tested under a continuous constant current density of 100 mA/cm^2. As exhibited in Fig. 7b, the potential almost did not increase after 20 h, suggesting superior stability. To further investigate the stability performance at high current densities, the chronopotentiometry was conducted at different current densities such as 500, 1000, and 2000 mA/cm^2 for a total of 30 h, as demonstrated in Fig. 7c. It can be seen clearly that the chronopotentiometric curve is flat at 500 and 1000 mA/cm^2. However, at a much higher current of 2000 mA/cm^2, the potential slightly increased. Our observation during the test was that the bubble generation was huge to obviously consume the electrolyte, leading to less contact of the electrodes with the electrolyte. Therefore, once we re-filled the electrolyte, the curve would move back to its normal position. Furthermore, the LSV curves before and after the high current stability test in Fig. S11 clearly overlap, indicating outstanding stability performance. The protrusions at high current densities of 1000 and 2000 mA/cm^2 (indicated

by the green circles in Fig. 7c) during a switch to a new test condition can be attributed to the slower kinetic mass transfer as the needed ions were massive. The protrusion phenomenon did not happen at low current densities, as revealed in Fig. S12. The actual amounts of hydrogen and oxygen gases were also quantitatively measured by a water-gas displacement approach. Fig. 7d demonstrates the hydrogen and oxygen production of MNF-2 under a constant current density of 100 mA/cm^2. The corresponding hydrogen and oxygen rates were 46.2 and 22.6 mL/h, respectively, which was very similar to the theoretical ratio of 2:1. Furthermore, the calculated Faradaic efficiency (FE) for both hydrogen and oxygen was near 100%. The Faradaic efficiencies of other MoNiFe catalysts are tabulated in Table S2. Table 3 compares the performance of our MNF-2 to that of previously reported bifunctional electrocatalysts. In the first six rows, the NiFeMo electrocatalysts are surveyed in the literature. Compared to the NiFeMo inverse-opals prepared by electrodeposition in ref. 43, our catalyst had a lower performance. Unfortunately, Pt foil with a smaller size than the working electrode was used as the counter electrode during the electrodeposition, which might have Pt trace contributed to their great HER performance. The trace amount of Pt is well known to significantly improve HER performance. Therefore, it is suggested in the community to use a larger area of Pt counter electrode to balance the charge on the working electrode [42]. The other ternary NiMoFe prepared by electrodeposition, hydrothermal followed by thermal reduction, and chemical vapor deposition (CVD) were comparable to our data. To have a fair comparison, the bifunctional electrocatalysts made by the sputtering technique and other routes are also surveyed, as listed in Table 3. The performance of our MNF-2 was quite comparable to those of recently reported
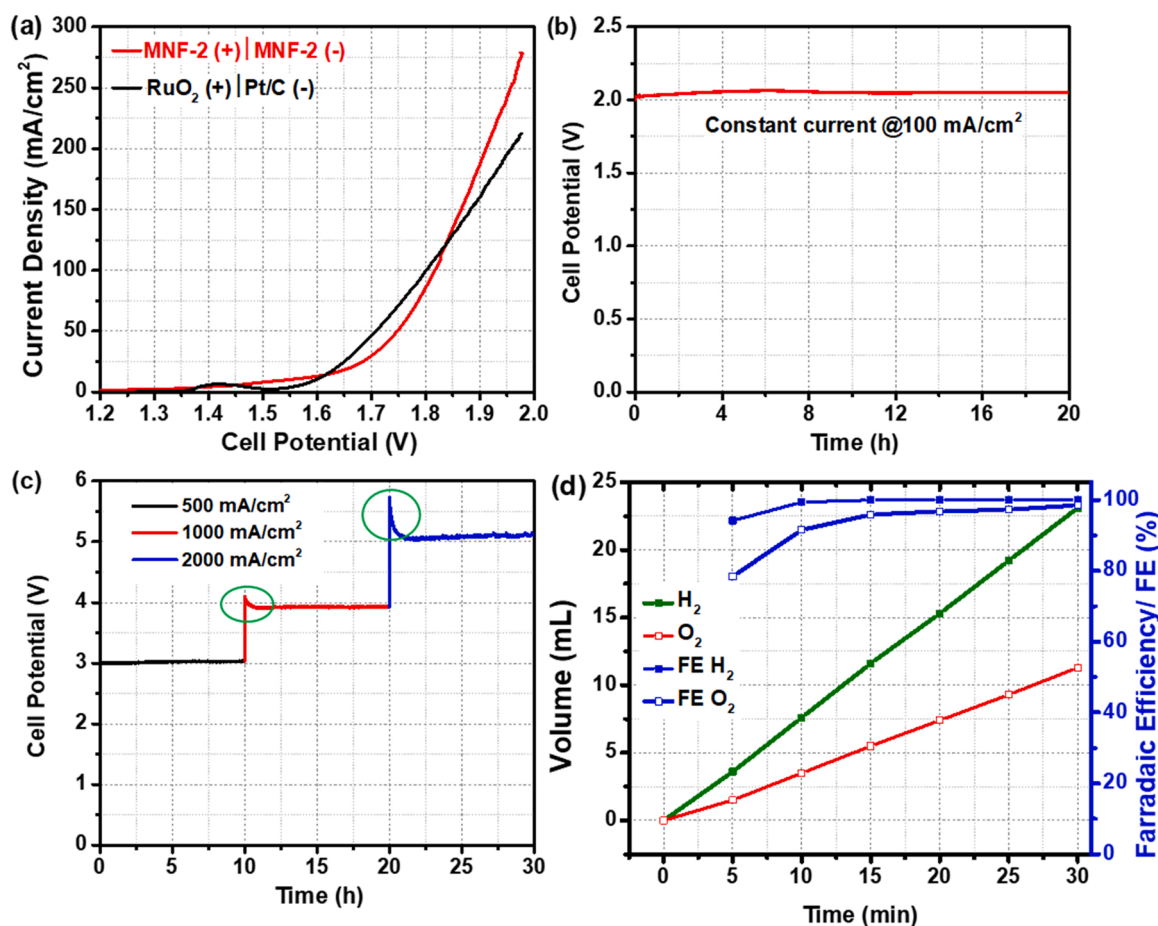

Fig. 7. (a) LSV of water splitting using MNF-2 as the cathode and anode (b) Stability test for 20 h by using a constant current technique, (c) Stability test at high current densities of 500, 1000, and 2000 mA/cm^2, and (d) Hydrogen (H_2) and oxygen (O_2) volume produced at a constant current of 100 mA/cm^2 and their corresponding faradaic efficiencies.

Table 3

Comparison of cell voltage of present work with some recently bifunctional electrocatalysts.

No.	Catalyst	Process	Cell voltage (V)		Ref.
			@ 10 mA/cm²	@ 100 mA/cm²	
1	MoNiFe thin film	Sputtering	1.55	1.82	*This work*
2	NiFeMo inverse-opals	Electrodeposition	1.47	1.62	[43]
3	NiFeMo	Electrodeposition	1.60	1.80	[44]
4	NiFeMo	Hydrothermal at 160 °C/6 h + reduction at 500 °C/1 h	1.45	1.84	[45]
5	MoNiFe/N-CNT	CVD for N-CNT + reduction at 400 °C/H₂ or hydrothermal sulfurization	1.58	1.85	[46]
6	NiMo M/O	Hydrothermal at 100 °C/4 h & 180 °C/10 h + reduction at 500 °C/2 h	1.53	–	[47]
7	FeCoNiCuPd	Sputtering	1.52	1.62	[48]
8	NiMo	Sputtering	1.57	–	[49]
9	NiFe/ZnO	Sputtering	1.60	1.90	[50]
10	Mn₂P-Mn₂O₃	Pyrolysis at 1150 °C/1 h, N₂ + Nafion paste	1.60	1.85	[51]
11	Co₃S₄/CeO₂	Co foam + hydrothermal at 180 °C/8 h	1.64	–	[52]
12	1 T-Co₄S₃-WS₂ /CC	Hydrothermal at 200 °C/8 h + Sulfurization at 500 °C/2 h	1.59	1.8	[53]
13	CoFeP/N-doped Carbon nanofiber	Pyrolysis at 800 °C/2 h + electrodeposition + phosphorization at 350 °C/2 h	1.59	1.9	[54]
14	Te/Fe-NiOOH	Soaking for 32 h + Hydrothermal at 180 °C/10 h	1.65	–	[55]
15	FeCoNi(S)	Hydrothermal at 140 °C/7 h + sulfurization at 160 °C/8 h	1.53	1.70	[56]
16	Sn₄P₃/Co₂P	Hydrothermal at 120 °C/10 h + phosphorization at 350 °C/2 h	1.56	1.80	[57]

catalysts, such as Mn₂P-Mn₂O₃, Co₃S₄/CeO₂, 1 T-Co₄S₃-WS₂, CoFeP/N-doped carbon nanofiber, Te/Fe-NiOOH, FeCoNi(S), and Sn₄P₃/Co₂P. Most of the available electrocatalysts for overall water splitting have been fabricated by hydrothermal method, pyrolysis, and electrodeposition. Fig. 8.
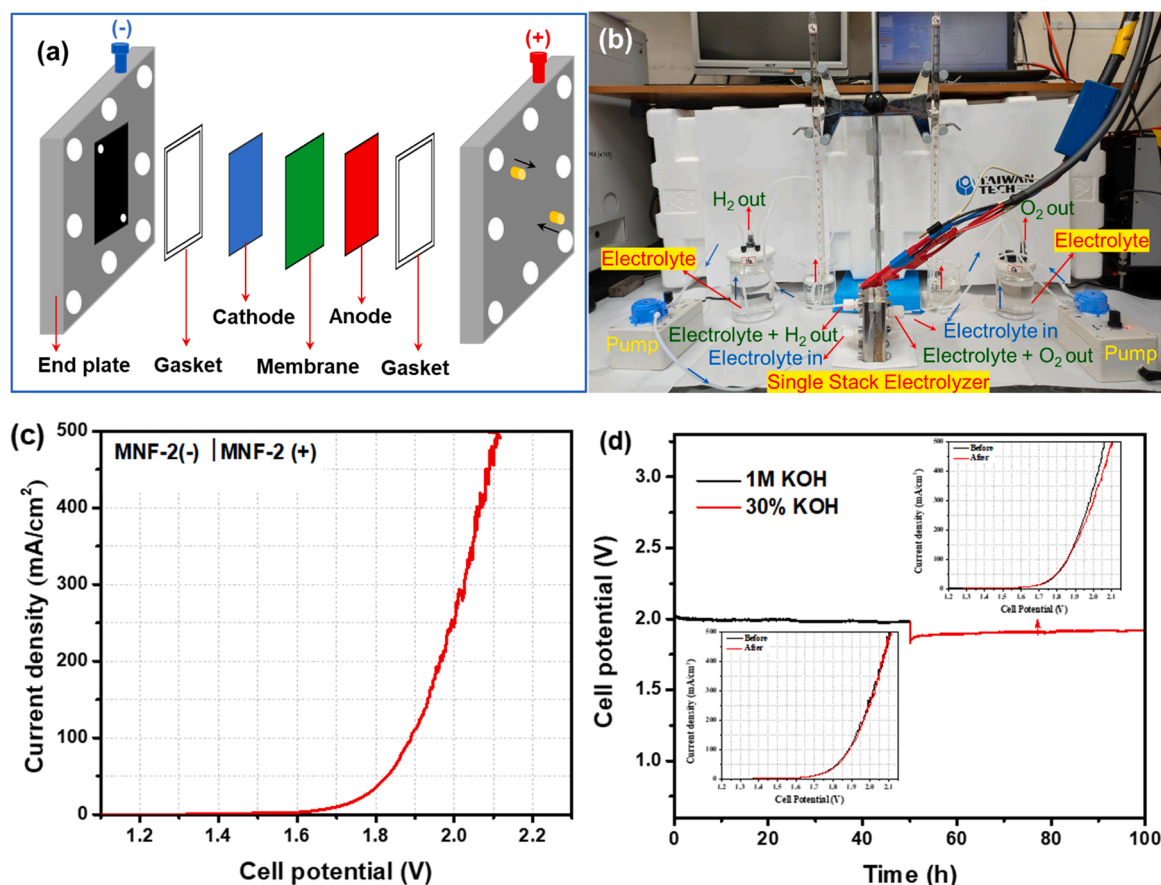
3.3.4. Single stack cell electrolysis

To evaluate the feasibility of our MNF-2 catalyst for potential commercialization, we further assembled a single stack cell for electrolysis by scaling up the geometrical electrode area from 1 cm² to 9 cm². Fig. 8a schematically illustrates the design of our single stack cell, consisting of two end plates, gaskets, cathode, membrane, and anode. The cell is much simpler as compared to the reported design [58]. The as-sputtered MNF-2 on nickel foam was directly used as the substrate and current collector without any binders to ensure excellent catalyst-to-substrate adhesion, as demonstrated by the mechanical peeling test using the scotch tape in Fig. S14. The gasket was placed near

the cathode and anode for gas/liquid tight, whereas a treated alkaline exchange membrane was installed in between the cathode and anode not only to separate the hydrogen and oxygen gases but also to transport the OH⁻ ions to the anode side. Fig. 8b exhibits a photograph of the experiment set-up for overall water splitting measurements in an alkaline solution. Two peristaltic pumps were used to inject electrolyte from the reservoirs into the anode and cathode at a constant flow rate of 120 mL/min. At first, we evaluated the performance of the MNF-2 catalyst cell in 1 M KOH electrolyte at room temperature by measuring the LSV at a potential window of 1.2–2.1 V. The LSV curve in Fig. 8c demonstrates that the cell potentials to reach high current densities at the industry level of 100 and 500 mA/cm² are 1.9 and 2.1 V, respectively. The resistance/barrier from the alkaline membrane contributed to a minor difference in cell potential as compared to the overall water splitting with a single cell without a membrane (1.82 V at 100 mA/cm²) in the previous section. To study the stability of our bifunctional catalyst, the MNF-2 cell was subjected to 1 M KOH for 50 h under a constant current of 900 mA or current density of 100 mA/cm². The plot of potential vs. time in Fig. 8b is nearly flat with no notable increase, demonstrating the outstanding stability performance of our MNF-2 cell. In addition, the LSV was also measured after a 50-hour stability test. The LSV curves before and after almost overlap (inset in Fig. 8d bottom), further indicating that the electrolytic performance has not degraded. The hydrogen and oxygen rates were then measured under a constant current density of 100 mA/cm² and the values were 398 and 194 mL/h, respectively, which corresponded to a nearly 100% Faradaic efficiency, as shown in Fig. S15. We further continued to evaluate the performance of the MNF-2 cell by changing the electrolyte solution to 30% KOH (about 6.9 M), which is commonly used as the standard electrolyte in the real application. The LSV curve demonstrates that cell potential at 100 mA/cm² is 1.85 V, slightly lower than in 1 M KOH (1.9 V) due to better ionic conductivity in the presence of a higher KOH concentration. The stability test was then continued for another 50 h (red line) under the same constant current density. It can be seen that the performance of our MNF-2 cell was quite stable without a significant change in potential as the test duration increased to 100 h. The LSV after stability test (inset in Fig. 8) only shows a slight degradation. The calculated cell efficiency of our single stack cell for electrolysis was about 62.5% (detailed calculation in supporting information). On the basis of these findings, it is highly believed that our sputtered MNF-2 thin-film catalyst has great potential to be used as bifunctional electrodes for a practical application in overall water splitting.

3.4. Post-characterizations

After bifunctional MNF-2 catalyst was used for stability test, it was washed several times and soaked in DI water for several hours to remove the KOH coating. After drying process, MNF-2 catalyst was then characterized using several characterization techniques, including SEM, Raman, XRD, and XPS. As exhibited in Fig. 9a, the morphology of MNF-2 catalyst after being used as the anode to perform the OER was totally different as compared to the fresh catalyst. Fig. 9a clearly exhibits the formation of the nanosheet structure, indicating the phase transformation occurred on the surface as a result of anodization in alkaline solution. The formation nano-sheet morphology after OER test in alkaline environment has been reported in the previous reports [45,59]. Both XRD and Raman analyses were also performed to identify the phase of that nanosheet. XRD analysis in Fig. S16 does not show any peak, indicating that the surface remains amorphous. However, Raman analysis in Fig. 9b clearly exhibits a peak at around 482 cm⁻¹. According to the previous study, the Raman peak at about 480 cm⁻¹ is related to the Ni-O vibration in the NiOOH phase [60]. Next, the XPS analysis was performed to confirm the surface chemistry. As shown in Fig. 9c, the high-resolution XPS of Mo 3d did not change except the shift of binding energy to a lower energy as compared to the fresh one. The binding energies of 228.5 and 231.5 eV correspond to the Mo° 3d₅/₂ and Mo°

Fig. 8. (a) Schematic illustration of electrolysis components in single stack cell, (b) Photograph of the experimental setup, (c) LSV curve of overall water splitting using MNF-2 as the cathode and anode, and (d) Stability test using a constant current density of 100 mA/cm^2 (900 mA) in 1 M KOH for 50 h, followed by another 50 h in 30% KOH.

$3d_{3/2}$, while the peaks at binding energies of 229.9 and 233.0 eV can be assigned as the Mo^{4+} $3d_{5/2}$ and Mo^{4+} $3d_{3/2}$. The two peaks at binding energies of 232.7 and 235.8 eV are assigned to Mo^{6+} $3d_{5/2}$ and Mo^{6+} $3d_{3/2}$, respectively. As demonstrated in Fig. 9d, the high resolution XPS spectrum of Ni 2p after OER was clearly different as compared to before it was used. The presence of Ni^{3+} clearly appears for the MNF-2 after being used for stability test. The binding energies at 855.9 and 873.3 eV are attributed to the spin orbitals of Ni^{3+} $2p_{3/2}$ and Ni^{3+} $2p_{1/2}$, respectively, which did not exist for the fresh MNF-2. This higher oxidation state occurs due to oxidation of Ni^{2+} or Ni^0. The ratio of metallic Ni over the Ni^{2+} and Ni^{3+} is about 0.92, which is lower than the value of 1.58 for MNF-2 before test due to the oxidation of Ni metal. The characteristic peak of Fe 2p in Fig. 9e was also similar for MNF-2 before and after the OER test. The spin orbitals of Fe$^\circ$ $2p_{3/2}$, Fe^{2+} $2p_{3/2}$, and Fe^{3+} $2p_{3/2}$ could be found at binding energies of 706.8, 708.6, and 711.52 eV, respectively. The shift in the binding energy of Mo, Ni, and Fe to a lower energy could be attributed to the changes in valence state. Hence, the XPS peaks of Ni significantly changed after OER, whereas the XPS peaks of Mo and Fe only shifted a little, indicating that Ni phase transition plays an important role in the OER. This finding is consistent with the Raman to confirm the presence of the in-situ grown NiOOH phase. With all this data in hand, we strongly believe that the active sites of the NiOOH (nickel oxyhydroxide) phase contribute to the excellent OER performance of MNF-2. It is also well known that metal oxyhydroxide could behave as the active catalyst for water oxidation in the electrocatalysis field [61]. On the contrast, MNF-2, after being used as the cathode for executing the HER, did not exhibit any significant morphological differences between its pre- and post-use states, as revealed in Fig. 9a. Moreover, Raman and XRD also confirm that there is no phase

transition. The XPS analysis in Fig. 9c-e shows that the characteristic high resolution XPS peaks of Mo 3d, Ni 2p, and Fe 2p are extremely comparable to those of MNF-2 before the HER test, showing that there is no change after the HER test. These results confirm that the MoNiFe alloy is responsible for the excellent HER performance. The main reason why the morphology of the MNF-2 did not change after the HER stability test was that there is no any phase transformation occurred due the metal-based catalyst is stable under reduction reaction. However, the metal-based MNF-2 can be oxidized during the OER stability test, leading to a phase transformation from metal to metal oxyhydroxide with the characteristic of a 2D nanosheet.

3.5. Electrocatalytic mechanism

Based on the surface morphology analyses depicted in Fig. 1, all the as-sputtered MoNiFe alloy with various Mo ratios possessed identically dense, flat, and smooth surfaces with no obvious differences. Their electrolytic HER and OER performance, however, were significantly different. Therefore, it is worth noting that the nanostructure or morphology with high geometric surface area is not a controlling factor for the electrocatalytic activity. The fine-tuning element composition at atomic level plays a vital role in determining the electrocatalytic performance. As revealed by the actual electrochemically active sites calculation in terms of ECSA in Table 2, the value of active sites dramatically increased by 4-fold after the addition of Mo. The HER performance in Fig. 5a also revealed a significant improvement after the incorporation of Mo atoms into the NiFe system, demonstrating that Mo atoms play a vital role in executing the HER. As evidenced by the Tafel analysis, the value greatly decreased from 161 to 73 mV/dec after
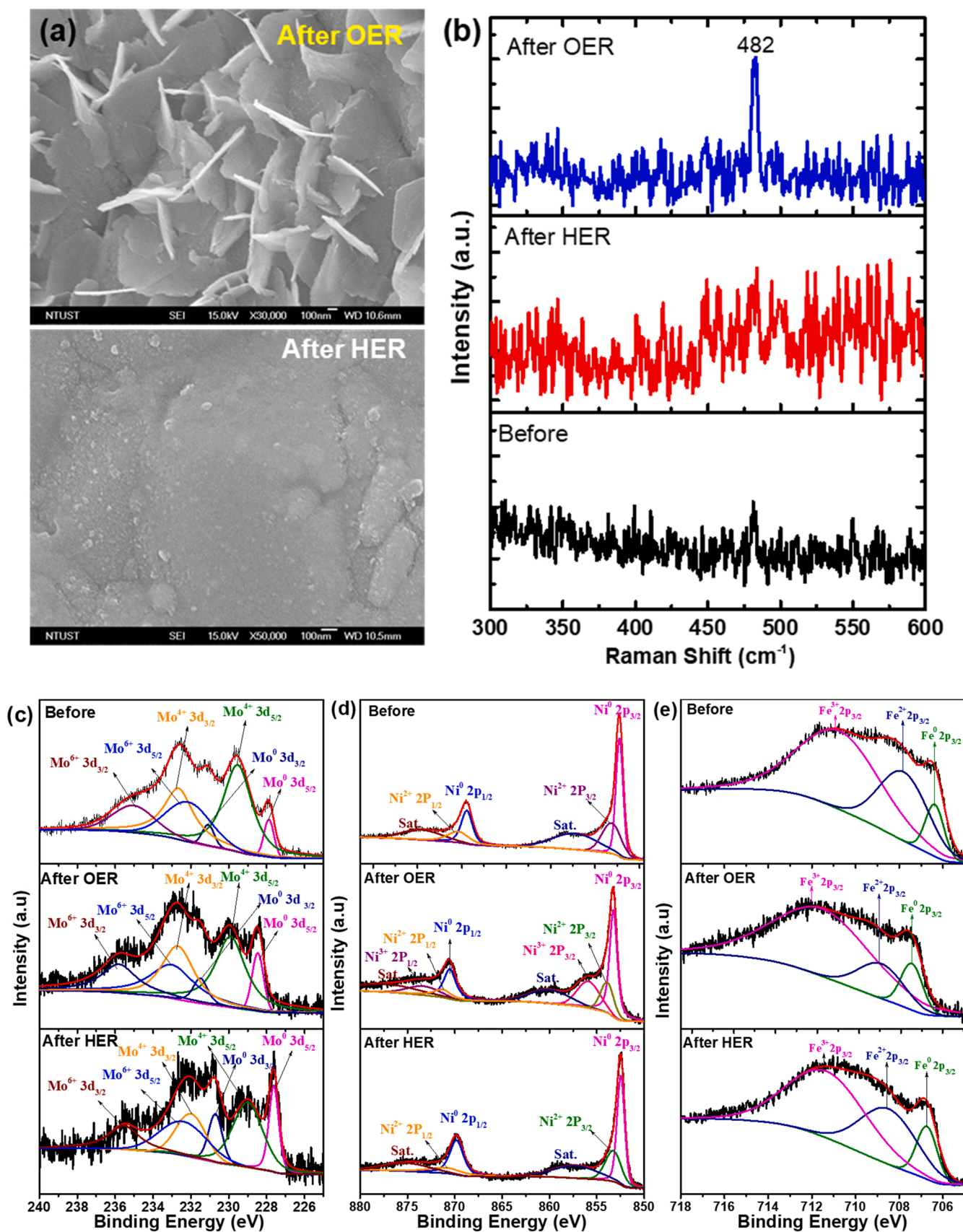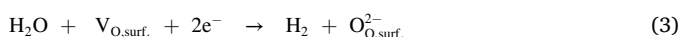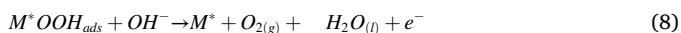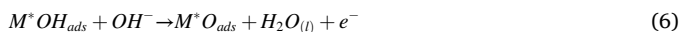
Fig. 9. Post-characterizations of (a) SEM images, (b) Raman spectra, and High resolution XPS spectra of (c) Mo, (d) Ni, and (e) Fe for MNF-2 before and after the OER and HER tests.

incorporating the optimum Mo ratio in the MNF-2 catalyst. The lower Tafel value indicates that there is an improvement in the HER kinetic by accelerating the water dissociation step to generate much more protons (H*). Without the addition of Mo in MNF-0 (NiFe), the water dissociation step is slow, leading to less proton generation. The Tafel value also suggests that the mechanism of hydrogen generation is generally controlled by the Volmer and Heyrovsky steps, as demonstrated in Eq. 1 and Eq. 2, respectively. The addition of Mo atoms is intended not only to improve water dissociation but also lower the free energy of hydrogen adsorption, as revealed by the previous computational calculations [13, 62]. As surface oxidation leads to the nonstoichiometric Fe_3O_{4-x} and MoO_y oxide compounds formed in the Ni matrix, the water dissociation can be aided by the oxygen vacancies in Fe_3O_{4-x} and MoO_y in Eq. 3 to attract the negatively charged oxygen in H_2O to weaken the O-H bonds, similar to photo HER kinetics [63].

$$H_2O + \quad e^- \rightarrow \quad H^* + \quad OH^- \tag{1}$$

$$H^* + H_2O + \quad e^- \rightarrow H_2 + \quad OH^- \tag{2}$$

$$H_2O + V_{O,surf.} + 2e^- \rightarrow H_2 + O^{2-}_{O,surf.} \tag{3}$$

The Tafel slope value can also be used to predict the mechanism of oxygen generation [64]. Our MNF-2 for OER had a small Tafel value of 33.8 mV/dec, indicating a favorable kinetic reaction involving multi-electron transfer. Although NiFe-based materials have long been recognized to be active catalysts for OER [65], our finding reveals that the addition of Mo atoms in the NiFe host can further improve the OER performance. As a result, our strategy of incorporating Mo atom into the NiFe system has successfully improved not just the HER but also the OER performance. The presence of surface oxygen vacancies is also important for OER activity to trap the hydroxide ions, as demonstrated in Eq. 4. Eqs. 5–8 illustrate the general mechanism of oxygen generation via multi-electron transfer. Initially, the hydroxide ions adsorb on the surface-active site of the catalyst (M*). The other hydroxides then bind to the M^*OH_{ads} to form M^*O_{ads} and to release a water molecule. M^*O_{ads} then react with the hydroxide ion to generate the OOH_{ads}. Lastly, after the reaction of OOH_{ads} with the hydroxide ion, oxygen is produced along with water. From the post-characterizations to show the existence of Ni^{3+} in NiOOH and the formation of nanosheets shape, the active species of M* is the Ni element in MNF-2 to execute the reversible Ni oxidation reaction, while the multivalent $Fe^\circ/Fe^{2+}/Fe^{3+}$ and $Mo^\circ/Mo^{4+}/Mo^{6+}$ elements in films provide the advantageous electron-transport path to provide high OER activity. With the reversible Ni oxidation in an alkaline solution for OER, the catalyst electrode is stable and protected by reversible oxyhydroxide layer.

$$V_O + OH^- \rightarrow HO_O + e^- \tag{4}$$

$$M^* + OH^- \rightarrow M^*OH_{ads} + e^- \tag{5}$$

$$M^*OH_{ads} + OH^- \rightarrow M^*O_{ads} + H_2O_{(l)} + e^- \tag{6}$$

$$M^*O_{ads} + OH^- \rightarrow M^*OOH_{ads} + e^- \tag{7}$$

$$M^*OOH_{ads} + OH^- \rightarrow M^* + O_{2(g)} + \quad H_2O_{(l)} + e^- \tag{8}$$

3.6. Surface composition design of MoNiFe trimetal

The sputtering thin-film technology has shown a great promise for the application in the electrocatalytic water splitting. The symmetric stack cell in the size of 3×3 cm^2 did not show any degradation after 100 h under the current density of 100 mA/cm^2. The excellent water splitting performance for the sputtered MoNiFe thin films with a dense and smooth morphology suggests that specific surface area is not a major concern issue. However, it is strongly related to the electrochemical active surface area (ECSA), as the ECSA value increased from 150 cm^2 to

575 cm^2 after adding 1.05% Mo into the NiFe for HER. With the XPS analysis, Mo is mainly in the form of Mo^{4+} and Mo^{6+}, Fe in the form of Fe^{3+}, and Ni in the form Ni°. The nonstoichiometric or partially oxidized Fe_3O_{4-x} and MoO_y oxide compounds in the Ni matrix are proposed for the oxidized surface of MoNiFe film. For HER, the positively charged Mo ions for Eq. 1 and the oxygen vacancies for Eq. 3 occur to attract the negatively charged oxygen in H_2O molecule to distort two O-H bonds in H_2O, to lead to the dissociation of H_2O, and to form H_2 gas. For OER, it involves the outwards-grown Ni oxidation layer for reversible reactions. However, if the whole surface is covered by Ni to form NiOOH, the electrode conductivity can become worse. Therefore, the oxides and Ni together on the oxidized surface are crucial to have good activity. Basically, the MoNiFe composition design is related to the surface oxidation to have Fe for Mo in $FeMo_{1-y}$ being easily oxidized into charge states, Mo^{4+}/Mo^{6+} for the H_2O absorption, oxygen vacancies of partially oxidized oxides for H_2O adsorption, and Ni for the reversible OER reaction. In other words, the existence of Fe activates the atomic Mo sites by phase transformation to facilitate water dissociation. With the atomic Mo site activation and surface composition, the performance of the all-sputtered MoNiFe full cell is understandable. At last, the sputtering thin-film technology has opened another path for the research of electrocatalytic water splitting to improve the interfacial/interphase adherence in considering the much larger bubble buoyant force at high current density.

4. Conclusions

A ternary MoNiFe alloy has been successfully developed by a magnetron sputtering thin-film technique. The as-sputtered MoNiFe alloy had an amorphous nature with a flat, smooth and compact surface. The films can be viewed as the clusters of FeMo-based intermetallic compounds in NiFe/Ni matrices. Both HER and OER performances in an alkaline electrolyte greatly improved after the incorporation of Mo into the NiFe system. The MNF-2 catalyst had the best performance, with a 2.8-fold active surface area, as compared to the Mo-free catalyst. That MNF-2 could act as a bifunctional electrocatalyst to drive the overall water splitting with a cell voltage of 1.55 V for a current density of 10 mA/cm^2. The feasibility study for practical scale-up application with a 3×3 cm^2 single stack cell electrolysis indicated that cell voltages of 1.9 and 2.1 V are required to achieve high current densities at the industrial level, such as 100 and 500 mA/cm^2, respectively. Our stack cell has reached an efficiency of 62.5%, is exceptionally stable for 100 h at 100 mA/cm^2, and generates hydrogen and oxygen at rates of 398 and 194 mL/h, respectively. How can a dense and smooth catalyst still work with excellence for both electrodes without peeling even operating at 500, 1000, and 2000 mA/cm^2 each for 10 h? The two important factors for HER are the Mo-site activation and the oxygen vacancy formation due to the Mo/Fe-aided partial surface oxidation. The major contribution to OER is from the surface-metallic Ni to execute the Ni/NiOOH oxidation, while other partially oxidized compounds enhance OER with oxygen vacancies to trap hydroxyl groups and keep providing electron transport paths. With the technology transfer of thin-film sputtering to grow stable electrocatalyst and the knowledge of surface composition design, the amorphous, dense, noble metal-free, and strongly bonded MoNiFe thin film is promising in electrocatalytic water splitting.

CRediT authorship contribution statement

Noto Susanto Gultom: Investigation, Writing – original draft, Validation, Visualization, **Tien-Shin Chen:** Investigation, Visualization. **Mikha Zefanya Silitonga:** Investigation, Visualization. **Dong-Hau Kuo:** Writing – review & editing, Conceptualization, Resources.

Declaration of Competing Interest

The authors declare that they have no known competing financial

interests or personal relationships that could have appeared to influence the work reported in this paper.

Data Availability

Data will be made available on request.

Acknowledgments

Appendix A. Supporting information

Supplementary data associated with this article can be found in the online version at doi:10.1016/j.apcatb.2022.122103.

References

[1] J. Li, Z. Zhu, Y. Huang, F. Wang, M.-S. Balogun, Ni3N: a multifunctional material for energy storage and electrocatalysis, Mater. Today Energy 26 (2022), 101001, https://doi.org/10.1016/j.mtener.2022.101001.
[2] Z.N. Zahran, E.A. Mohamed, Y. Tsubonouchi, M. Ishizaki, T. Togashi, M. Kurihara, K. Saito, T. Yui, M. Yagi, Electrocatalytic water splitting with unprecedentedly low overpotentials by nickel sulfide nanowires stuffed into carbon nitride scabbards, Energy Environ. Sci. 14 (2021) 5358–5365, https://doi.org/10.1039/D1EE00509J.
[3] X. Li, L. Zhao, J. Yu, X. Liu, X. Zhang, H. Liu, W. Zhou, Water splitting: from electrode to green energy system, Nanomicro Lett. 12 (2020) 131, https://doi.org/10.1007/s40820-020-00469-3.
[4] X. Li, J.Y. Yu, J. Jia, A.Z. Wang, L.L. Zhao, T.L. Xiong, H. Liu, W.J. Zhou, Confined distribution of platinum clusters on MoO2 hexagonal nanosheets with oxygen vacancies as a high-efficiency electrocatalyst for hydrogen evolution reaction, Nano Energy 62 (2019) 127–135, https://doi.org/10.1016/j.nanoen.2019.05.013.
[5] X.W. Yu, J. Zhao, M. Johnsson, Interfacial engineering of nickel hydroxide on cobalt phosphide for alkaline water electrocatalysis, Adv. Funct. Mater. 31 (2021) 2101578, https://doi.org/10.1002/adfm.202101578.
[6] N.S. Gultom, H. Abdullah, C.N. Hsu, D.H. Kuo, Activating nickel iron layer double hydroxide for alkaline hydrogen evolution reaction and overall water splitting by electrodepositing nickel hydroxide, Chem. Eng. J. 419 (2021), 129608, https://doi.org/10.1016/j.cej.2021.129608.
[7] T. Xiong, B. Huang, J. Wei, X. Yao, R. Xiao, Z. Zhu, F. Yang, Y. Huang, H. Yang, M. S. Balogun, Unveiling the promotion of accelerated water dissociation kinetics on the hydrogen evolution catalysis of NiMoO4 nanorods, J. Energy Chem. 67 (2022) 805–813, https://doi.org/10.1016/j.jechem.2021.11.025.
[8] P. Xu, J. Li, J. Luo, L. Wei, D. Zhang, D. Zhou, W. Xu, D. Yuan, (Fe0.2Ni0.8)0.96S tubular spheres supported on Ni foam as an efficient bifunctional electrocatalyst for overall water splitting, Sci. Rep. 8 (2018) 9425, https://doi.org/10.1038/s41598-018-27477-z.
[9] F. Yang, T. Xiong, P. Huang, S. Zhou, Q. Tan, H. Yang, Y. Huang, M.S. Balogun, Nanostructured transition metal compounds coated 3D porous core-shell carbon fiber as monolith water splitting electrocatalysts: a general strategy, Chem. Eng. J. 423 (2021), 130279, https://doi.org/10.1016/j.cej.2021.130279.
[10] X. Li, Q. Hu, H. Yang, T. Ma, X. Chai, C. He, Bimetallic two-dimensional materials for electrocatalytic oxygen evolution, Chin. Chem. Lett. 33 (2022) 3657–3671, https://doi.org/10.1016/j.cclet.2021.12.001.
[11] Z.W. Seh, J. Kibsgaard, C.F. Dickens, I. Chorkendorff, J.K. Norskov, T.F. Jaramillo, Combining theory and experiment in electrocatalysis: Insights into materials design, Science 355 (2017) eaad4998, https://doi.org/10.1126/science.aad4998.
[12] S.H. Yu, D.H.C. Chua, Toward high-performance and low-cost hydrogen evolution reaction electrocatalysts: nanostructuring cobalt phosphide (CoP) particles on carbon fiber paper, ACS Appl. Mater. Interfaces 10 (2018) 14777–14785, https://doi.org/10.1021/acsami.8b02755.
[13] Z. He, J. Zhang, Z. Gong, H. Lei, D. Zhou, N. Zhang, W. Mai, S. Zhao, Y. Chen, Activating lattice oxygen in NiFe-based (oxy)hydroxide for water electrolysis, Nat. Commun. 13 (2022) 2191, https://doi.org/10.1038/s41467-022-29875-4.
[14] J. Liang, Q. Liu, T.S. Li, Y.L. Luo, S.Y. Lu, X.F. Shi, F. Zhang, A.M. Asiri, X.P. Sun, Magnetron sputtering enabled sustainable synthesis of nanomaterials for energy electrocatalysis, Green. Chem. 23 (2021) 2834–2867, https://doi.org/10.1039/D0GC03994B.
[15] H. Zhou, F. Yu, Q. Zhu, J. Sun, F. Qin, L. Yu, J. Bao, Y. Yu, S. Chen, Z. Ren, Water splitting by electrolysis at high current densities under 1.6 volts, Energy Environ. Sci. 11 (2018) 2858–2864, https://doi.org/10.1039/C8EE00927A.
[16] G. Qian, J. Chen, T. Yu, L. Luo, S. Yin, N-doped graphene-decorated NiCo alloy coupled with mesoporous NiCoMoO NAno-sheet heterojunction for enhanced water electrolysis activity at high current density, Nanomicro Lett. 13 (2021) 77, https://doi.org/10.1007/s40820-021-00607-5.
[17] H. Abdullah, N.S. Gultom, C.C. Hsu, H. Shuwanto, D.H. Kuo, Amorphous-Ni(OH) (2) on a vertically grown lamellar Ag-modified MoSx thin-film electrode with surface defects for hydrogen production in alkaline solutions, ACS Appl. Energy Mater. 4 (2021) 3869–3880, https://doi.org/10.1021/acsaem.1c00252.
[18] K. Wasa, Sputtering phenomena, in: K. Wasa, I. Kanno, H. Kotera (Eds.), Handbook of Sputtering Technology, William Andrew Publishing, Oxford, 2012, pp. 41–75.
[19] B.M. Lynch, Z.C. Wang, L. Ma, E.M. Paschalidou, F. Wiame, V. Maurice, P. Marcus, Passivation-induced Cr and Mo enrichments of 316L stainless steel surfaces and effects of controlled pre-oxidation, J. Electrochem. Soc. 167 (2020), 141509 doi.org/10.1149.1945-7111/abc727.
[20] C. Peng, M. Shi, F. Li, Y. Wang, X. Liu, H. Liu, Z. Li, Construction of 1T@2H MoS2 heterostructures in situ from natural molybdenite with enhanced electrochemical performance for lithium-ion batteries, RSC Adv. 11 (2021) 33481–33489, https://doi.org/10.1039/D1RA05565H.
[21] M.L. Hu, Z.N. Wang, M.L. Li, C.G. Guo, L.P. Li, Nanosheet MoS2-decorated MoO2 on porous carbon as electrodes for efficient hydrogen evolution, ACS Appl. Nano Mater. 5 (2022) 8175–8183, https://doi.org/10.1021/acsanm.2c01272.
[22] X. Wang, B. Zhang, W. Zhang, M. Yu, L. Cui, X. Cao, J. Liu, Super-light Cu@Ni nanowires/graphene oxide composites for significantly enhanced microwave absorption performance, Sci. Rep. 7 (2017) 1584, https://doi.org/10.1038/s41598-017-01529-2.
[23] S. Wang, Y. Li, J. Yang, T. Wang, B. Yang, Q. Cao, X. Pu, L. Etgar, J. Han, J. Zhao, X. Li, A. Hagfeldt, Critical role of removing impurities in nickel oxide on high-efficiency and long-term stability of inverted perovskite solar cells, Angew. Chem. Int. Ed. 61 (2022), e202116534, https://doi.org/10.1002/anie.202116534.
[24] M. Yuan, C. Nan, Y. Yang, G. Sun, H. Li, S. Ma, Uniform FexNiy nanospheres: cost-effective electrocatalysts for nonaqueous rechargeable Li-O2 batteries, ACS Omega 2 (2017) 4269–4277, https://doi.org/10.1021/acsomega.7b00497.
[25] Z. Wang, J. Ang, J. Liu, X.Y.D. Ma, J. Kong, Y. Zhang, T. Yan, X. Lu, FeNi alloys encapsulated in N-doped CNTs-tangled porous carbon fibers as highly efficient and durable bifunctional oxygen electrocatalyst for rechargeable zinc-air battery, Appl. Catal. B 263 (2020), 118344, https://doi.org/10.1016/j.apcatb.2019.118344.
[26] T. Yonezawa, 2.08 - Nickel alloys: properties and characteristics, in: R.J.M. Konings (Ed.), Comprehensive Nuclear Materials, Elsevier, Oxford, 2012, pp. 233–266.
[27] K.J. Miller, M. Sofman, K. McNerny, M.E. McHenry, Metastable γ-FeNi nanostructures with tunable Curie temperature, J. Appl. Phys. 107 (2010) 09A305, https://doi.org/10.1063/1.3334198.
[28] A.Fa Guillermet, The Fe−Mo (Iron−Molybdenum) system, Bull. Alloy Ph. Diagr. 3 (1982) 359–367, https://doi.org/10.1007/BF02869315.
[29] J.H. Nam, M.J. Jang, H.Y. Jang, W. Park, K. Wang, S.M. Choi, B. Cho, Room-temperature sputtered electrocatalyst WSe2 nanomaterials for hydrogen evolution reaction, J. Energy Chem. 47 (2020) 107–111, https://doi.org/10.1016/j.jechem.2019.11.027.
[30] Z. Ma, Z. Li, S. Li, P. Li, H. Zhang, Nanostructured Ni2N thin films magnetron-sputtered on nickel foam as efficient electrocatalyst for hydrogen evolution reaction, Mater. Lett. 229 (2018) 148–151, https://doi.org/10.1016/j.matlet.2018.07.016.
[31] N.S. Gultom, D.H. Kuo, H. Abdullah, C.N. Hsu, Fabrication of an Ag2S-MoSx/MoNiAg film electrode for efficient electrocatalytic hydrogen evolution in alkaline solution, Mater. Today Energy 21 (2021), 100768, https://doi.org/10.1016/j.mtener.2021.100768.
[32] A.T.A. Ahmed, A.S. Ansari, S.M. Pawar, B. Shong, H. Kim, H. Im, Anti–corrosive FeO decorated CuCo2S4 as an efficient and durable electrocatalyst for hydrogen evolution reaction, Appl. Surf. Sci. 539 (2021), 148229, https://doi.org/10.1016/j.apsusc.2020.148229.
[33] S.M. Pawar, A.T. Aqueel Ahmed, C.H. Lee, P.T. Babar, J.H. Kim, S.U. Lee, H. Kim, H. Im, Experimental and theoretical insights into transition-metal (Mo, Fe) codoping in a bifunctional nickel phosphide microsphere catalyst for enhanced overall water splitting, ACS Appl. Energy Mater. 4 (2021) 14169–14179, https://doi.org/10.1021/acsaem.1c02930.
[34] H.L.S. Santos, P.G. Corradini, M. Medina, J.A. Dias, L.H. Mascaro, NiMo-NiCu inexpensive composite with high activity for hydrogen evolution reaction, ACS Appl. Mater. Interfaces 12 (2020) 17492–17501, https://doi.org/10.1021/acsami.0c00262.
[35] Y. Gao, T. Xiong, Y. Li, Y. Huang, Y. Li, M.S.J.T. Balogun, A simple and scalable approach to remarkably boost the overall water splitting activity of stainless steel electrocatalysts, ACS Omega 4 (2019) 16130–16138, https://doi.org/10.1021/acsomega.9b02315.
[36] F. Bao, E. Kemppainen, I. Dorbandt, F. Xi, R. Bors, N. Maticiuc, R. Wenisch, R. Bagacki, C. Schary, U. Michalczik, P. Bogdanoff, I. Lauermann, R. van de Krol, R. Schlatmann, S. Calnan, Host, suppressor, and promoter—the roles of Ni and Fe on oxygen evolution reaction activity and stability of NiFe alloy thin films in alkaline media, ACS Catal. 11 (2021) 10537–10552, https://doi.org/10.1021/acscatal.1c01190.
[37] A. Grimaud, O. Diaz-Morales, B. Han, W.T. Hong, Y.-L. Lee, L. Giordano, K. A. Stoerzinger, M.T.M. Koper, Y. Shao-Horn, Activating lattice oxygen redox reactions in metal oxides to catalyse oxygen evolution, Nat. Chem. 9 (2017) 457–465, https://doi.org/10.1038/nchem.2695.
[38] A.T.A. Ahmed, S.M. Pawar, A.I. Inamdar, H. Im, H. Kim, Fabrication of FeO@CuCo2S4 multifunctional electrode for ultrahigh-capacity supercapacitors and efficient oxygen evolution reaction, Int. J. Energy Res. 44 (2020) 1798–1811, https://doi.org/10.1002/er.5027.

[39] G. Solomon, M.G. Kohan, M. Vagin, F. Rigoni, R. Mazzaro, M.M. Natile, S. You, V. Morandi, I. Concina, A. Vomiero, Decorating vertically aligned MoS2 nanoflakes with silver nanoparticles for inducing a bifunctional electrocatalyst towards oxygen evolution and oxygen reduction reaction, Nano Energy 81 (2021) 105664, https://doi.org/10.1016/j.nanoen.2020.105664.

[40] A.I. Inamdar, H.S. Chavan, S.M. Pawar, H. Kim, H. Im, NiFeCo oxide as an efficient and sustainable catalyst for the oxygen evolution reaction, Int. J. Energy Res. 44 (2020) 1789–1797, https://doi.org/10.1002/er.5026.

[41] C. Maccato, L. Bigiani, L. Girardi, A. Gasparotto, O.I. Lebedev, E. Modin, D. Barreca, G.A. Rizzi, Plasma-assisted synthesis of Co3O4-based electrocatalysts on Ni foam substrates for the oxygen evolution reaction, Adv. Mater. Interfaces 8 (2021) 2100763, https://doi.org/10.1002/admi.202100763.

[42] C. Wei, R.R. Rao, J. Peng, B. Huang, I.E.L. Stephens, M. Risch, Z.J. Xu, Y. Shao-Horn, Recommended practices and benchmark activity for hydrogen and oxygen electrocatalysis in water splitting and fuel cells, Adv. Mater. 31 (2019) 1806296, https://doi.org/10.1002/adma.201806296.

[43] C.T. Hsieh, C.L. Huang, Y.A. Chen, S.Y. Lu, NiFeMo alloy inverse-opals on Ni foam as outstanding bifunctional catalysts for electrolytic water splitting of ultra-low cell voltages at high current densities, Appl. Catal. B 267 (2020), 118376, https://doi.org/10.1016/j.apcatb.2019.118376.

[44] Z.H. Lv, Z.H. Li, X. Tan, Z.M. Li, R. Wang, M.J. Wen, X. Liu, G.X. Wang, G.W. Xie, L. H. Jiang, One-step electrodeposited NiFeMo hybrid film for efficient hydrogen production via urea electrolysis and water splitting, Appl. Surf. Sci. 552 (2021), 149514, https://doi.org/10.1016/j.apsusc.2021.149514.

[45] F. Qin, Z. Zhao, M.K. Alam, Y. Ni, F. Robles-Hernandez, L. Yu, S. Chen, Z. Ren, Z. Wang, J. Bao, Trimetallic NiFeMo for overall electrochemical water splitting with a low cell voltage, ACS Energy Lett. 3 (2018) 546–554, https://doi.org/10.1021/acsenergylett.7b01335.

[46] R.J. Zhao, X.S. Liu, K. Deng, W. Tian, K. Ma, S. Tan, H.R. Yue, J.Y. Ji, Trimetallic Mo-/Ni-/Fe-based hybrids anchored on hierarchical N-CNTs arrays with abundant defects and interfaces for alkaline water splitting, Ind. Eng. Chem. Res. 60 (2021) 12559–12569, https://doi.org/10.1021/acs.iecr.1c01806.

[47] M. Zhou, Y.F. Zeng, Y. Liu, Y. Sun, F. Lu, X.Y. Zhang, R.X. Cao, Y.X. Xue, X.H. Zeng, Y.P. Wu, Ni-Mo based metal/oxide heterostructured nanosheets with largely exposed interfacial atoms for overall water-splitting, Appl. Surf. Sci. 597 (2022), 153597, https://doi.org/10.1016/j.apsusc.2022.153597.

[48] S. Wang, B. Xu, W. Huo, H. Feng, X. Zhou, F. Fang, Z. Xie, J.K. Shang, J. Jiang, Efficient FeCoNiCuPd thin-film electrocatalyst for alkaline oxygen and hydrogen evolution reactions, Appl. Catal. B 313 (2022), 121472, https://doi.org/10.1016/j.apcatb.2022.121472.

[49] J. Sun, B. Yu, F. Tan, W. Yang, G. Cheng, Z. Zhang, High throughput preparation of Ni–Mo alloy thin films as efficient bifunctional electrocatalysts for water splitting, Int. J. Hydrog. Energy 47 (2022) 15764–15774, https://doi.org/10.1016/j.ijhydene.2022.03.065.

[50] Y. Luo, Y. Wu, D. Wu, C. Huang, D. Xiao, H. Chen, S. Zheng, P.K. Chu, NiFe-layered double hydroxide synchronously activated by heterojunctions and vacancies for the oxygen evolution reaction, ACS Appl. Mater. Interfaces 12 (2020) 42850–42858, https://doi.org/10.1021/acsami.0c11847.

[51] X. Wang, G. Huang, Z. Pan, S. Kang, S. Ma, P.K. Shen, J. Zhu, One-pot synthesis of Mn2P-Mn2O3 heterogeneous nanoparticles in a P, N -doped three-dimensional porous carbon framework as a highly efficient bifunctional electrocatalyst for overall water splitting, J. Chem. Eng. 428 (2022), 131190, https://doi.org/10.1016/j.cej.2021.131190.

[52] Z. Feng, J. Pu, M. Liu, W. Zhang, X. Zhang, L. Cui, J. Liu, Facile construction of hierarchical Co3S4/CeO2 heterogeneous nanorod array on cobalt foam for electrocatalytic overall water splitting, J. Colloid Interface Sci. 613 (2022) 806–813, https://doi.org/10.1016/j.jcis.2022.01.081.

[53] Q. Peng, X. Shao, C. Hu, Z. Luo, T. Taylor Isimjan, Z. Dou, R. Hou, X. Yang, Co4S3 grafted 1 T-phase dominated WS2 ultrathin nanosheet arrays for highly efficient overall water splitting in alkaline media, J. Colloid Interface Sci. 615 (2022) 577–586, https://doi.org/10.1016/j.jcis.2022.02.031.

[54] B. Wei, G. Xu, J. Hei, L. Zhang, T. Huang, Q. Wang, CoFeP hierarchical nanoarrays supported on nitrogen-doped carbon nanofiber as efficient electrocatalyst for water splitting, J. Colloid Interface Sci. 602 (2021) 619–626, https://doi.org/10.1016/j.jcis.2021.06.045.

[55] S. Ibraheem, X. Li, S.S.A. Shah, T. Najam, G. Yasin, R. Iqbal, S. Hussain, W. Ding, F. Shahzad, Tellurium triggered formation of Te/Fe-NiOOH nanocubes as an efficient bifunctional electrocatalyst for overall water splitting, ACS Appl. Mater. Interfaces 13 (2021) 10972–10978, https://doi.org/10.1021/acsami.0c22573.

[56] L. Chen, Y.P. Wang, X. Zhao, Y.C. Wang, Q. Li, Q.C. Wang, Y.G. Tang, Y.P. Lei, Trimetallic oxyhydroxides as active sites for large-current-density alkaline oxygen evolution and overall water splitting, J. Mater. Sci. Technol. (2022) 128–135, https://doi.org/10.1016/j.jmst.2021.08.083.

[57] X. Qin, X. Yan, D. Kim, Z. Teng, T. Chen, J. Choi, L. Xu, Y. Piao, Interfacial engineering and hydrophilic/aerophobic tuning of Sn4P3/Co2P heterojunction nanoarrays for high-efficiency fully reversible water splitting, Appl. Catal. B. 304 (2022) 120923, https://doi.org/10.1016/j.apcatb.2021.120923.

[58] X. Yan, J. Biemolt, K. Zhao, Y. Zhao, X. Cao, Y. Yang, X. Wu, G. Rothenberg, N. Yan, A membrane-free flow electrolyzer operating at high current density using earth-abundant catalysts for water splitting, Nat. Commun. 12 (2021) 4143, https://doi.org/10.1038/s41467-021-24284-5.

[59] N.S. Gultom, C.-H. Li, D.-H. Kuo, H. Abdullah, Single-step synthesis of Fe-Doped Ni3S2/FeS2 nanocomposites for highly efficient oxygen evolution reaction, ACS Appl. Mater. Interfaces 14 (2022) 39917–39926, https://doi.org/10.1021/acsami.2c08246.

[60] P.W. Menezes, S. Yao, R. Beltran-Suito, J.N. Hausmann, P.V. Menezes, M. Driess, Facile access to an active gamma-NiOOH electrocatalyst for durable water oxidation derived from an intermetallic nickel germanide precursor, Angew. Chem. Int. Ed. 60 (2021) 4640–4647, https://doi.org/10.1002/anie.202014331.

[61] Z. Yu, Y. Bai, G. Tsekouras, Z. Cheng, Recent advances in Ni-Fe (Oxy)hydroxide electrocatalysts for the oxygen evolution reaction in alkaline electrolyte targeting industrial applications, Nano Sel. 3 (2021) 766–791, https://doi.org/10.1002/nano.202100286.

[62] Y.N. Zhou, W.H. Hu, Y.N. Zhen, B. Dong, Y.W. Dong, R.Y. Fan, B. Liu, D.P. Liu, Y. M. Chai, Metallic MoOx layer promoting high-valence Mo doping into CoP nanowires with ultrahigh activity for hydrogen evolution at 2000 mA cm(-2), Appl. Catal. B 309 (2022), 121230, https://doi.org/10.1016/j.apcatb.2022.121230.

[63] N.S. Gultom, H. Abdullah, D.-H. Kuo, Phase transformation of bimetal zinc nickel oxide to oxysulfide photocatalyst with its exceptional performance to evolve hydrogen, Appl. Catal. B 272 (2020), 118985, https://doi.org/10.1016/j.apcatb.2020.118985.

[64] N.T. Suen, S.F. Hung, Q. Quan, N. Zhang, Y.J. Xu, H.M. Chen, Electrocatalysis for the oxygen evolution reaction: recent development and future perspectives, Chem. Soc. Rev. 46 (2017) 337–365, https://doi.org/10.1039/C6CS00328A.

[65] J. Mohammed-Ibrahim, A review on NiFe-based electrocatalysts for efficient alkaline oxygen evolution reaction, J. Power Sources 448 (2020), 227375, https://doi.org/10.1016/j.jpowsour.2019.227375.